ACSNANO

ARTICLE

Strong, Ultralight Nanofoams with Extreme Recovery and Dissipation by Manipulation of Internal Adhesive Contacts

Sei Jin Park, Jungho Shin, Daniel J. Magagnosc, Sanha Kim, Changhong Cao, Kevin T. Turner, Prashant K. Purohit, Daniel S. Gianola, and Anastasios John Hart*

Cite This: https://dx.doi.org/10.1021/acsnano.0c02422

Read Online

| ACCESS | | 📊 Metrics & More | | 📖 Article Recommendations | | SI Supporting Information |

ABSTRACT: Advances in three-dimensional nanofabrication techniques have enabled the development of lightweight solids, such as hollow nanolattices, having record values of specific stiffness and strength, albeit at low production throughput. At the length scales of the structural elements of these solids—which are often tens of nanometers or smaller—forces required for elastic deformation can be comparable to adhesive forces, rendering the possibility to tailor bulk mechanical properties based on the relative balance of these forces. Herein, we study this interplay via the mechanics of ultralight ceramic-coated carbon nanotube (CNT) structures. We show that ceramic-CNT foams surpass other architected nanomaterials in density-normalized strength and that, when the structures are designed to minimize internal adhesive interactions between CNTs, more than 97% of the strain after compression beyond densification is recovered. *Via* experiments and modeling, we study the dependence of the recovery and dissipation on the coating thickness, demonstrate that internal adhesive contacts impede recovery, and identify design guidelines for ultralight materials to have maximum recovery. The combination of high recovery and dissipation in ceramic-CNT foams may be useful in structural damping and shock absorption, and the general principles could be broadly applied to both architected and stochastic nanofoams.

KEYWORDS: *nanostructure, ceramic, foam, strength, damping, adhesive*
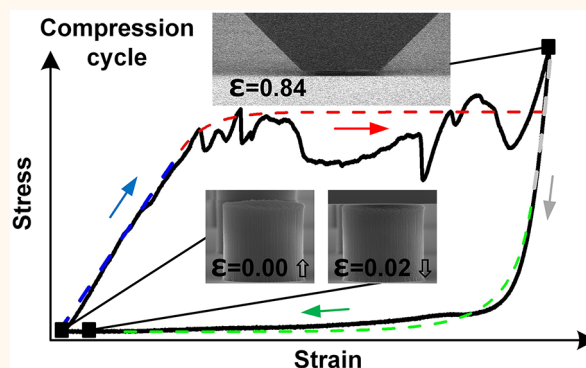
Ultralow density materials such as foams, aerogels, and micro/nano-lattices are of broad interest for their exceptional density-normalized mechanical properties and large surface areas and have many potential applications including as tissue scaffolds, thermal insulation, adsorbents, catalyst supports, battery electrodes, and flexible conductors.[1−8] Much recent effort has shown that mechanical properties of these materials can be tuned by geometric design and materials selection. For instance, as the dimensions of lattice structures[9,10] decrease to the nanoscale, mechanical behaviors such as flaw tolerance,[11] supercompressibility,[12,13] high recovery,[14] and flexibility of ceramic materials[15] arise.

Such structure-driven mechanical behaviors provide interesting opportunities to create materials with unusual combinations of properties, for instance, being stiff and dissipative simultaneously.[16] Hollow micro- and nanolattices are typically fabricated by high-resolution three-dimensional (3D) photo-patterning (e.g., using two photon lithography or the self-propagating photopolymer waveguides method), followed by coating and dissolution of the scaffold. Atomic layer deposition (ALD) of alumina has been used widely to reinforce ultralow density materials, tuning their mechanical properties such as stiffness, strength, and failure mechanism.[17−19] These hollow trusses represent unprecedented structural control and the above-mentioned properties including record high modulus/density ratios, but they presently lack scalability to much larger volumes due to the multiple steps involved and the low throughput of 3D photopatterning processes.

Moreover, in nanolattices, there is a general trade-off between recovery and damping; thin ceramic walls required

A
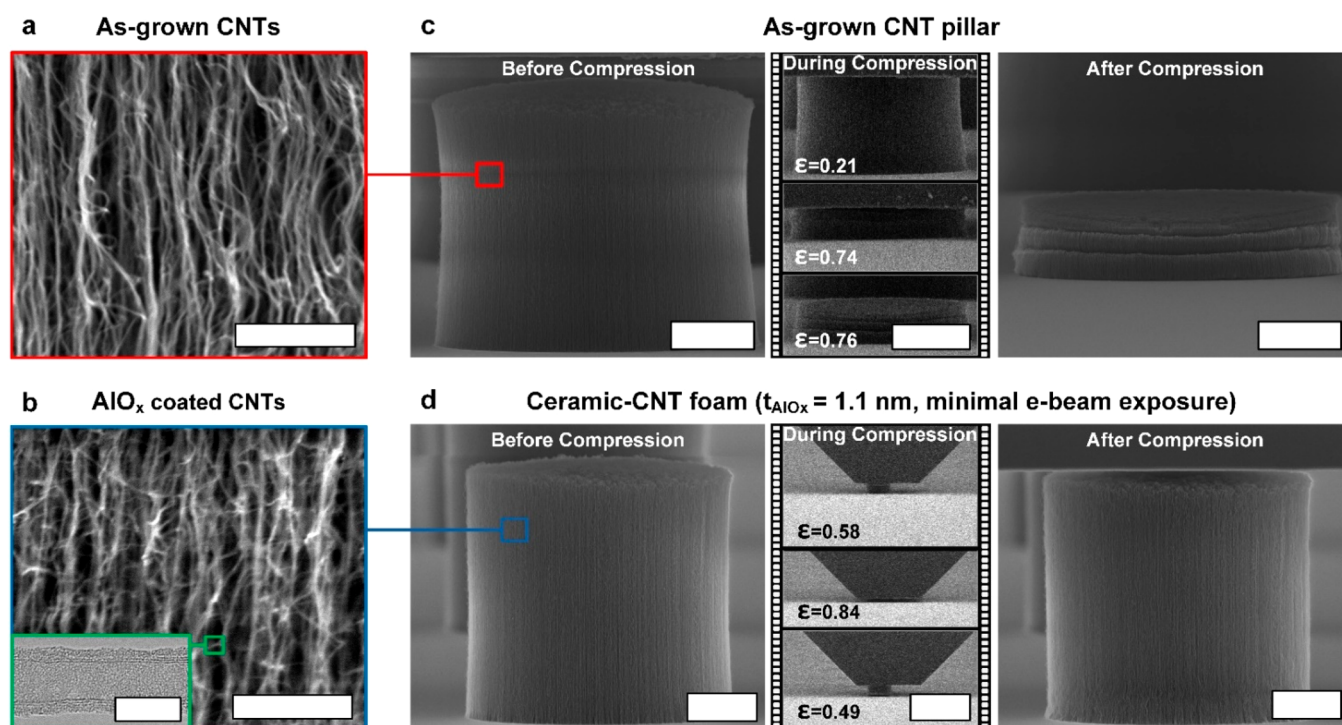
Figure 1. Morphology of as-grown (bare) CNT forest and ceramic-CNT foams: (a) an SEM image of bare CNTs, scale bar = 500 nm; (b) an SEM image of alumina-coated CNTs, with the inset showing a TEM image of a single alumina-coated CNT, scale bar = 500 nm, inset scale bar = 10 nm; (c) compression of as-grown CNT pillars exhibiting poor recovery, scale bar = 5 μm (before), 10 μm (during), and 5 μm (after); and (d) compression of ceramic-CNT foams, exhibiting exceptional recovery, scale bar = 5 μm (before), 50 μm (during), and 5 μm (after). In (d), e-beam exposure was minimized by reducing the magnification during compression and unloading.

to achieve recovery do not exhibit stiffness and strength needed for large energy absorption and dissipation. At a limit, adhesive energy can influence dissipation, but it is challenging to fabricate foams with struts whose adhesive forces upon self-contact is equivalent to the forces required for elastic deformation to significant strains. Instead, on the one hand, thin hollow struts are used, but ceramic thin films fracture upon large deformations necessary for strut−strut contact. On the other hand, materials built from organized nanowires or nanotubes—often having diameter in the ∼1−100 nm range— can potentially enter this interesting regime. In particular, carbon nanotubes (CNTs) can recover from extreme deformations and can be organized into hierarchical assemblies by chemical vapor deposition (CVD). And, perhaps owing to this intrinsic competition, the mechanical behavior of CNT networks can vary widely according to the density, diameter, and orientation of the CNTs.[12,20]

Herein, we study the interplay of elastic and adhesive energies in governing the mechanical behavior of ultralight solids, via ceramic-CNT foams created by coating CNT forests, in micropillar geometries, with ultrathin ceramic layers. We find that ceramic-CNT foams with ultrathin coatings exhibit mechanical behavior governed by the competition between elastic and adhesive forces and exhibit exceptional recovery from compression when the CNT−CNT adhesive interactions are reduced due to the surface properties of the coating. The critical role of adhesive forces in the mechanical response is understood by considering the balance of elastic restoring forces on deformed CNTs and the van der Waals (VDW) interaction forces between CNTs in contact. The load−unload cycles of the foams are modeled by treating the CNT network as a material that undergoes a transition between low density (rarified) and densified (compressed) phases. We find that the recovery of compressed foam depends on the strain rate and apparent charge on the struts, identifying the balance of elastic and adhesive forces as a versatile means of engineering the mechanics of ultralow density materials.

RESULTS AND DISCUSSION

Micropillars of ceramic-coated CNTs (ceramic-CNT foams) are used to investigate the coupling between elastic and adhesive energies in governing the dissipation and recovery of ultralow density materials. Arrays of CNT micropillars are first synthesized by atmospheric pressure CVD on a patterned thin-film catalyst substrate.[21] As the volume fraction of CNTs within the forest is low (∼10s of mg/cm³ range[22]), conformal coating of the CNTs provides an opportunity to tune the mechanical properties while preserving the hierarchical structure.[18]

As-grown CNT pillars have flat tops and straight sidewalls and are composed of individual CNTs that are intertwined with a vertically oriented texture. Scanning electron microscope (SEM) images of as-grown CNT pillars and ceramic-coated CNT pillars (foams) are shown in Figure 1. The diameter and height of the pillars were chosen to ensure that the ALD coating precursors fully penetrate the structure at the deposition conditions used.[18] After ALD, the CNTs are clad with an amorphous layer of alumina (Figures 1b and S2−S5). Using ozone as the oxidizer in the ALD process improved coating nucleation on the CNT surfaces and gave more conformal and uniform coatings. High-resolution transmission electron microscopy (HRTEM) reveals that the CNTs are ∼10 nm in diameter (Figure 1b, inset).[22] After two ALD cycles, the CNTs are partially covered with rough alumina (Figure S2).

This is to be expected, as the size of trimethylaluminum (TMA) molecules does not allow full coverage of the surface. Beyond five cycles, the alumina coating on the CNTs becomes continuous, and the roughness decreases as the coating thickness increases (Figures S3−S5). The alumina coating thicknesses were measured to be $t_{AlOx} = 1.1$, 2.1, and 5.3 nm for 5, 10, and 20 cycles, respectively (Table S1).

In situ SEM imaging during compression allowed for observation of structural changes of CNT pillars and ceramic-CNT foams at various strain rates ($\dot{\varepsilon} = 10^{-1}$/s, 10^{-2}/s, and 10^{-3}/s). In Figure 1c,d we show images of a CNT pillar and a ceramic-CNT foam ($t_{AlOx} = 1.1$ nm) before and after compression ($\dot{\varepsilon} = 10^{-1}$ /s). Upon compression, the CNT pillar initially deforms elastically, while strain is localized at the base due to the native density gradient of CNTs within the pillar.[23,24] Both structures were loaded to over 80% compressive strain; after compression, the CNT pillar remains in the deformed (compressed) state, wherein the ceramic-CNT foam recovers almost fully to the original undeformed state, with only a single crease on the sidewall. Notably, we observed that exposure to the electron beam in the SEM influences recovery (Figures S6 and S7), and therefore, experiments were performed with the electron beam off.

Exemplary compressive stress−strain (σ−ε) curves of CNT pillars and ceramic-CNT foams ($\dot{\varepsilon} = 10^{-1}$/s) are shown in Figure 2a. In all cases, the response is initially linear, then at a certain threshold strain, buckling of the CNT network occurs from the base of the pillar upward, keeping the stress values relatively constant, while the strain increases (plateau region). Once the compressive strain reaches a large enough value that the buckled struts pack against one other, the stress increases rapidly (densification regime). The coating thickness clearly influences the recovery and envelope area of the load−unload cycle.

The σ−ε curves of CNT pillars and ceramic-CNT foams show an expected increase in both compressive modulus and plateau stress with increasing coating thickness. The initial loading slope is used to represent the compressive modulus (E) and increase from 8.62 ± 0.18 MPa for as-grown CNT pillars to 14.0 ± 0.3, 20.2 ± 1.8, and 42.1 ± 2.6 MPa for CNT pillars coated with 1.1, 2.1, and 5.3 nm of alumina, respectively. The first abrupt change in loading slope was used to represent the compressive strength (σ_y), which increases from 0.90 ± 0.11 MPa for as-grown CNT pillars to 1.62 ± 0.64, 2.95 ± 0.75, and 4.02 ± 0.38 MPa, for CNT pillars coated with 1.1, 2.1, and 5.3 nm of alumina, respectively. This definition of compressive strength results in values that are in some cases significantly lower than the plateau stress, and therefore, the energy absorbed during compression is larger than a simple prediction using the yield stress in the elastic−perfectly plastic model.

The maximum stress before the first load drop is used to mark the onset of the plateau region. Within the plateau region, the bare CNT pillars undergo progressive buckling whereby the stress rises, until it reaches the plateau stress, at which point another buckle is initiated. The buckles propagate throughout the structure as the compression continues.[23] For $t_{AlOx} = 1.1$ and 2.1 nm, the sustained stress after the onset of the plateau is lower than the plateau stress, showing a valley between the initial linear elastic and densification regimes. For $t_{AlOx} = 5.3$ nm, the plateau stress has a slight overall positive slope. The change in the shape of stress−strain curves as the coating thickness increases is analogous to the effect of

increasing the relative density of the foam described in classical foam theory.[25] When unloaded, the stress reaches negative
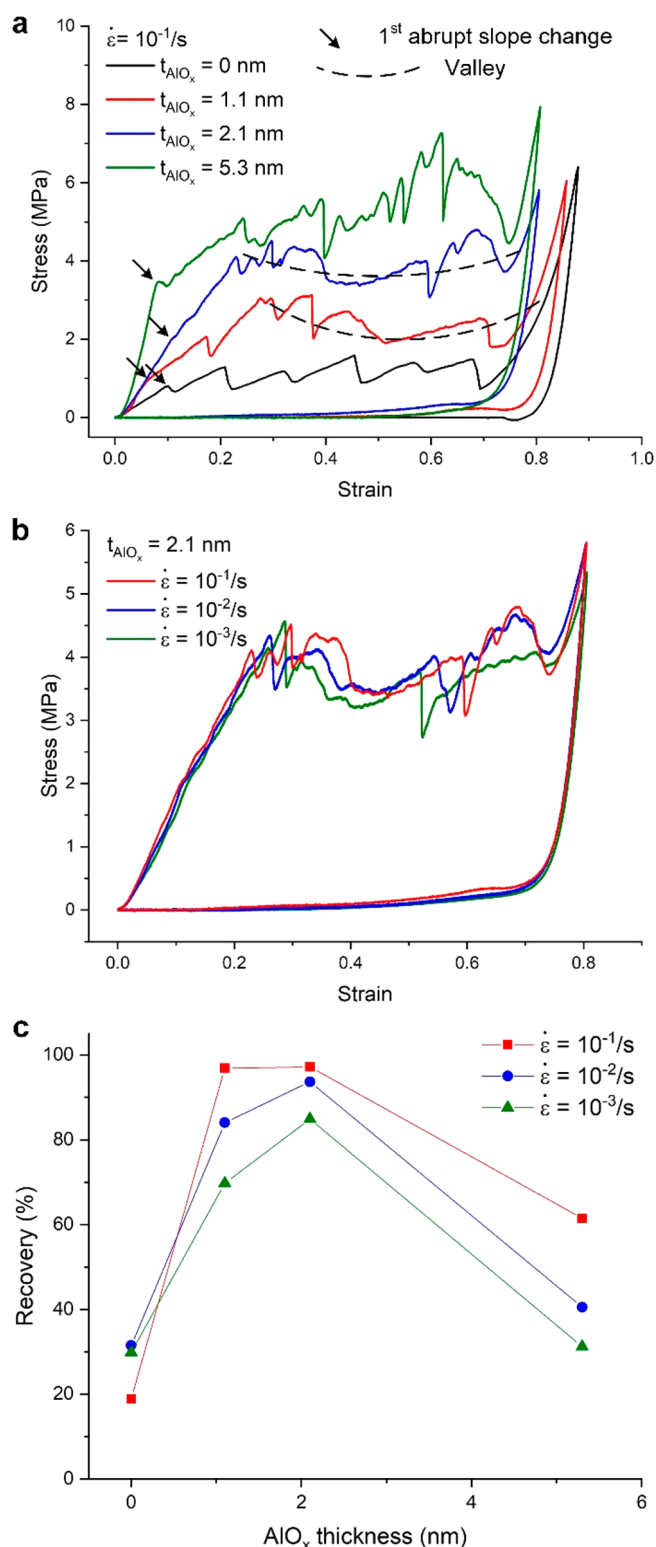
Figure 2. (a) Stress−Strain curves for bare CNT forest and ceramic-CNT foams ($t_{AlOx} = 1.1$, 2.1, and 5.3 nm) compressed at 10^{-1}/s. (b) Stress−Strain curves for ceramic-CNT foams ($t_{AlOx} = 1.1$ nm) compressed at 10^{-1}/s, 10^{-2}/s, and 10^{-3}/s. (c) Recovery of bare CNT forest and ceramic-CNT foams ($t_{AlOx} = 1.1$, 2.1, and 5.3 nm) compressed at 10^{-1}/s, 10^{-2}/s, and 10^{-3}/s. Maximum recovery occurs at $t_{AlOx} = 2.1$ nm across all loading rates.

values for as-grown CNT pillars, implying that CNTs adhere to the indenter tip and require small amounts of tensile stress to detach as the punch recedes from the pillar. The unloading curves of ceramic-CNT foams do not show this behavior, providing evidence that the alumina coating weakens the surface adhesion of the CNTs. Surface pull-off force measurements using an atomic force microscope on CNT pillars and ceramic-CNT foams confirm that the alumina coating reduces adhesive forces (Figures S8 and S9). This low intrinsic adhesion enables extreme recovery of the ceramic-CNT foams owing to the resilience of the CNTs themselves.[26−28]

The central role of adhesive forces in mediating mechanical behavior of the composite foams implies the potential influence of time scales, that is, strain rate. At fixed coating thickness of t_{AlOx} = 2.1 nm, the stress−strain curves are nearly invariant with strain rates from 10^{-1}/s to 10^{-3}/s, including the initial slope, the onset of the plateau, the densification strain, and even the magnitude and strain of the load drops (Figure 2b). These tests were done on neighboring pillars grown in an array on a single substrate, also indicating interestingly how the complex morphology of the CNT network leads to distinct features in the mechanical response.

Yet, strain rate has a significant effect on the recovery, and recovery is maximized at higher strain rates (Figures 2c and S10). The extent of recovery, $R = (\varepsilon_{max} - \varepsilon_{res})/\varepsilon_{max}$, was calculated from the SEM images, where ε_{max} is the maximum compressive strain reached, and ε_{res} is the residual strain after the indenter tip has separated from the top of the CNT pillars. For t_{AlOx} = 1.1 and 2.1 nm ceramic-CNT foams, the recovery reaches values of 96.9% and 97.2%, respectively (Figure 2c) at $\dot{\varepsilon} = 10^{-1}$/s. Compared to less than 40% recovery of as-grown CNT pillars, the improvements to above 95% recovery are striking. The recovery also depends strongly on the coating thickness and increases as the coating thickness increases, reaching the maximum at t_{AlOx} = 2.1 nm for all strain rates tested. For t_{AlOx} = 5.3 nm, we suspect the alumina layer fractures due to the high strains, and hence recovery from compression is diminished. The dependence of recovery on strain rate is consistent with prior studies of CNT forests following compression and supports the idea that the formation of nanoscale adhesive contact is time-dependent,[29] for instance, by zipping or sliding of CNTs in contact with one another.[30]

The ability of the foams to recover from extreme deformation is hypothesized to relate to the balance between elastic restoring forces acting on the deformed struts and the VDW surface interaction forces between the struts in contact. To compare the forces, we consider a simplified unit cell comprising of two wavy but generally aligned CNT segments (Figure 3a). Unit cell dimensions and other parameters are estimated based on small-angle X-ray scattering, as explained in the Supporting Information. The elastic restoring force (P) for a deformed CNT can be expressed using simply supported beams with one free end, by adding contributions from the CNT core and the alumina coating

$$P = \frac{12\pi\nu[E_1(r_2^4 - r_1^4) + E_2(r_3^4 - r_2^4)]}{h^3} \quad (1)$$

where ν is the deflection, E_1 and E_2 are Young's moduli of CNTs and alumina, respectively, r_1, r_2, and r_3 are CNT inner radius, CNT outer radius (equal to the coating inner radius), and the coating outer radius, respectively, and h is the height of
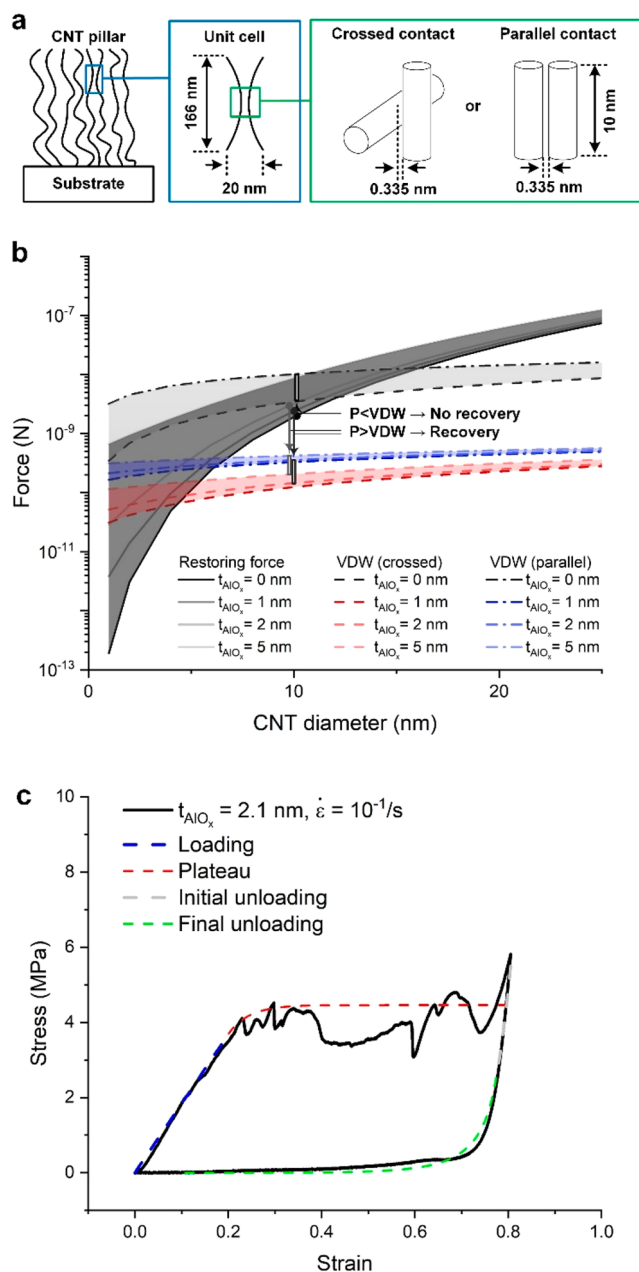
Figure 3. (a) CNT unit cell schematic showing two limiting cases of contact: crossed CNTs and parallel CNTs. (b) Comparison of elastic restoring force and van der Waals interaction force for CNT diameters of 1−40 nm and alumina coating thicknesses of 0−5 nm. (c) Fitting of an exemplary stress−strain curve of a ceramic-CNT foam with the phase transition model discussed in the text.

the unit cell (corresponding to the length of the undeformed CNTs). Following Israelachvili,[31] the VDW forces between cylinder pairs can be obtained using the derivative of the interaction energy with respect to the separation. Two limiting cases of crossed ($F_{VDW,c}$) and parallel ($F_{VDW,p}$) cylinder contacts are considered

$$F_{VDW,c} = -\frac{AR}{6D^2} \quad (2)$$

$$F_{VDW,p} = -\frac{AL\sqrt{R}}{16D^{2.5}} \quad (3)$$

Table 1. Summary of Fitted Mobility Parameters and Threshold Stresses and Corresponding Residual Strains and Recovery

AlO_x (nm)	strain rate (s^{-1})	M_{LH} ($MPa^{-1}\ s^{-1}$)	M_{HL} ($MPa^{-1}\ s^{-1}$)	σ_{LH} (MPa^{-1})	σ_{HL} (MPa^{-1})	ε_{res}	R_{model}
0	10^{-1}	0.9		1.0		0.79	7.1
1.1	10^{-1}	0.23	0.4	2.25	0.44	0.61	28.2
2.1	10^{-1}	0.4	0.08	3.7	2.52	0.36	55
5.3	10^{-1}	0.2	0.2	4.4	1.09	0.48	40
0	10^{-2}	0.9		1.0		0.61	28.2
1.1	10^{-2}	0.23	0.4	2.25	0.07	0.67	21.1
2.1	10^{-2}	0.4	0.08	3.7	0.28	0	100
5.3	10^{-2}	0.2	0.2	4.4	0.14	0.69	13.8
0	10^{-3}	0.9		1.0		0.73	14.1
1.1	10^{-3}	0.23	0.4	2.25	0.02	0.77	9.4
2.1	10^{-3}	0.4	0.08	3.7	0.06	0	100
5.3	10^{-3}	0.2	0.2	4.4	0.05	0.72	10

where A is the Hamaker constant, R is the cylinder radius, D is the separation between cylinders in contact, and L is the length of the parallel contact. Using eqs 1−3, the ratios of the restoring forces to VDW forces can be expressed as follows

$$\left| \frac{P}{F_{VDW,c}} \right| = \frac{72\pi}{A} \left[\frac{\nu D^2}{h^3} \left(E_2 r_3^{\,3} + \frac{(E_1 - E_2) r_2^{\,4} - E_1 r_1^{\,4}}{r_3} \right) \right]$$

(4)

$$\left| \frac{P}{F_{VDW,p}} \right| = \frac{192\pi}{A} \left[\frac{\nu D^{2.5}}{Lh^3} \left(E_2 r_3^{\,3.5} + \frac{(E_1 - E_2) r_2^{\,4} - E_1 r_1^{\,4}}{\sqrt{r_3}} \right) \right]$$

(5)

The deformed cylinder pairs in contact will separate upon unloading when these ratios exceed unity (i.e., $P > F_{VDW}$). It is readily seen that smaller Hamaker constant (A), increased stiffness (E_1 and E_2), and strut diameters (r_2 and r_3) are beneficial for recovery. Holding materials and strut dimensions constant, larger deflection (ν) and contact separation (D) will aid recovery, whereas larger unit cell height (h) and contact length (L) will hinder it. The implications are that sparse struts (larger deflection) that have rough surface morphology (larger contact separation) that are less aligned (smaller unit cell height and contact length) lead to greater recovery.

Following this approximation, the force balance for a range of CNT diameter (1−40 nm) coating thickness (and 0−5 nm) is shown in Figure 3b. By this model, we find that the high recovery is enabled by the lower intrinsic adhesion of the surfaces, even when CNT diameters are small. Specifically, the model predicts that the restoring force outweighs the interaction force at ∼14 nm diameter for bare CNTs. When ultrathin ceramic coatings (∼1 nm) are applied, the interaction force is reduced, and the restoring force starts overcoming the interaction force at ∼5 nm CNT diameter. Thus, the materials fabricated herein (using ∼10 nm diameter CNTs) transition from no recovery to high recovery by application of ultrathin coatings and efficiently maximize elastic energy storage along with dissipation provided by maximizing the relative contact strength. For thicker coatings, CNT diameters required to overcome the interaction forces are smaller, or conversely, the difference between elastic restoring forces and interaction forces is larger for a given CNT diameter. This trend is clear in experimental results shown in Figure 2c (except at $t_{AlOx} = 5.3$ nm, where we suspect that the alumina has fractured). Above 16 nm CNT diameter, the stored elastic energy outweighs the interaction even for the "stickiest" bare CNTs regardless of the contact configuration. While the threshold for this crossover would vary according to the exact dimensions and morphology of the CNTs and coating, its existence is consistent with previous reports of large recovery after compression for forests with 40 nm or larger diameter CNTs[12,32] and when CNT diameters are increased by CVD postgrowth deposition of amorphous carbon.[20]

The stress−strain behavior of the ceramic-CNT foams can be further understood using a phase change model,[33] which treats the compression, specifically the accumulation of buckled CNTs, as a transition between a low density (rarified) phase and a densified (compressed) phase. The model fits a nucleation stress and a mobility parameter value to each phase, which represent the threshold stress at which the other phase starts nucleating and how fast the phase boundary evolves. The fitted mobility parameters (M_{LH}, M_{HL}) and nucleation stresses (σ_{LH}, σ_{HL}) of the phase boundary are summarized in Table 1. For CNT pillars, M_{HL} and σ_{HL} were omitted due to the unloading curve reaching zero stress before the unloading plateau begins.

The stress−strain curves calculated using the fitted mobility parameters and threshold stresses capture the experimental results well (Figures 3c, S11, and 12). In general, higher σ_{HL} and lower M_{HL} are correlated with high recovery. A high σ_{HL} indicates that a larger fraction of the structure has transformed back into the rarified phase when unloading is complete. The inverse correlation with M_{HL} can be qualitatively explained by noting that M_{HL} is an indication of how fast the phase transition evolves; hence, at a fixed strain rate of unloading, the stresses reach zero before much recovery occurs. This relationship can be analytically described as (see Supporting Information for more details)

$$\varepsilon_{res} = \varepsilon^{HL} + \frac{\dot{\delta}}{E M_{HL} \gamma_T^{\,2}} \log \frac{\sigma_r^{HL}}{\sigma_r^{HL} - \sigma^{HL}}$$

(6)

where ε_{res} is the residual strain, ε^{HL} is the strain at which the rarified phase nucleates, $\dot{\delta} = \dot{\varepsilon}L$ is the displacement rate (negative for unloading) given by the product of strain rate ($\dot{\varepsilon}$) and pillar height (L), E is the Young's modulus, γ_T is the transformation strain (∼0.7 for pillars/foams used in this study), σ_r^{HL} is the stress at which the nucleated phase boundary moves (linearly related to σ^{HL}). For a given ε^{HL}, the ε_{res} is smaller when M_{HL} is smaller or $\dot{\varepsilon}$ is larger. While the model cannot precisely predict the amount of recovery according to the experiments, it predicts maximum recovery occurring at $t_{Alox} = 2.1$ nm, which matches the data.
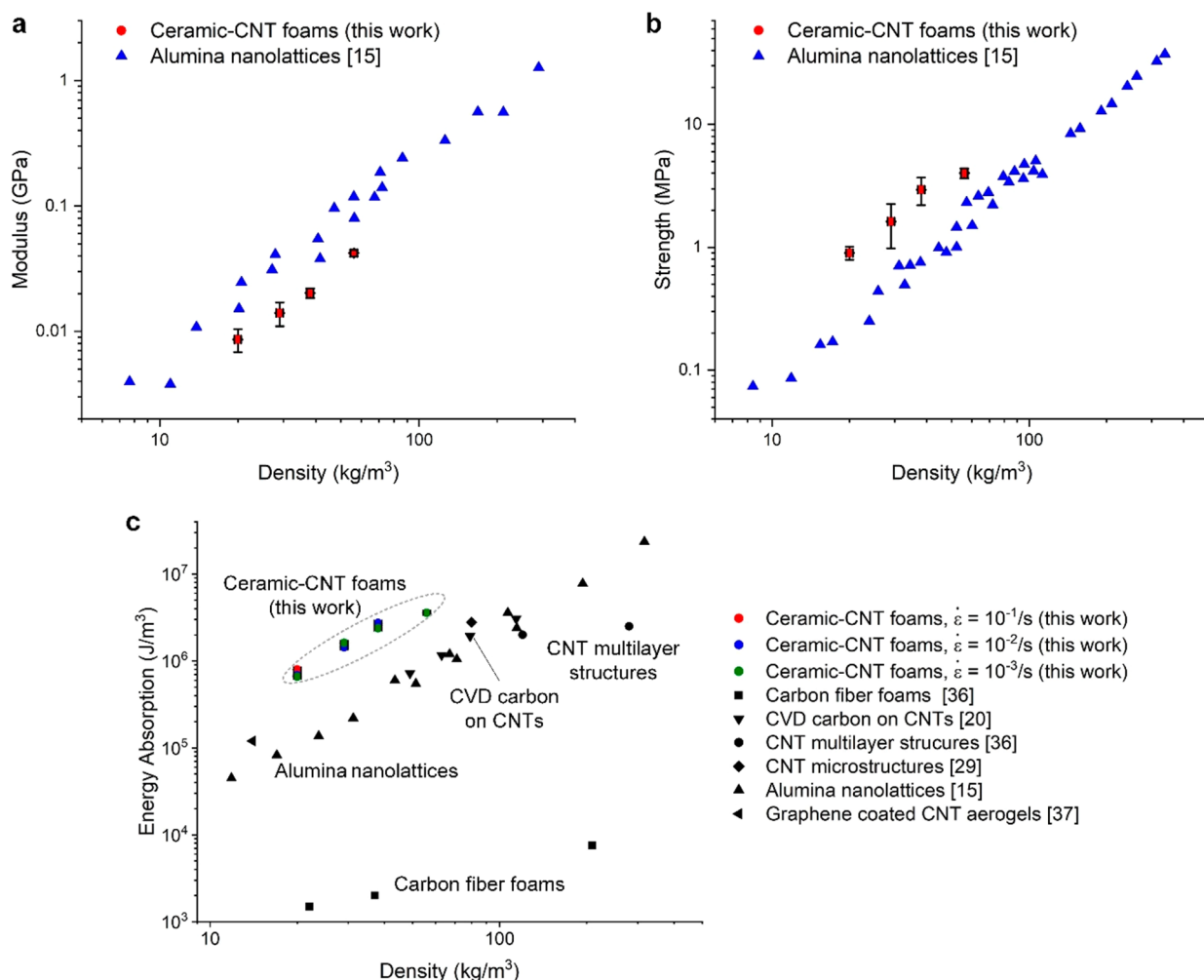
Figure 4. Material property space for bare CNT forests and ceramic-CNT foams compared to other ultralight nanostructured materials: (a) Compressive modulus vs density. (b) Compressive strength vs density. (c) Volume normalized energy absorption vs density. Notably, the CNT-ceramic foams described herein have comparable modulus along with higher strength and energy absorption than previously studied ultralightweight solids including hollow ceramic nanolattices and other CNT-based solids.

Finally, the compressive properties of the ceramic-CNT foams are compared to previously reported low-density materials. The bulk density of the materials could not be directly measured due to their small volume as well as their very low density. Instead the density was obtained by measuring the mass of coated larger-area CNT forests and normalizing by the volume of the CNT forest obtained from the catalyst area and SEM height measurements. By this approach, we find, on the one hand, the modulus-density range (Figure 4a) of the ceramic-CNT foams is comparable with hollow nanolattices;[15] the initial loading slope was used to calculate the modulus of our foams. On the other hand, the strength of ceramic-CNT foams exceeds low-density ceramic lattices by approximately 2−3-fold at comparable density (Figure 4b). This is because the ceramic-coated CNTs have much greater thickness-to-diameter ratios than hollow ceramic lattices, whose diameter is limited by the use of a sacrificial 3D printed template. The favorable geometry of the ceramic-CNT foams suppresses the shell buckling of individual struts[15,34] and presents a costrengthening effect of the CNT core and the ceramic outer layer.[17]

The modulus and strength of ceramic-CNT foams scale with density as $E \approx \rho^{1.58}$ and $\sigma_y \approx \rho^{1.49}$, respectively. Thus, the ceramic-CNT foams do not follow classical stiffness scaling ($E \approx \rho^2$) for open-cell foams but are bending-dominated ($\sigma_y \approx \rho^{1.5}$).[25] While the stochastic nature of CNT forests' internal structures makes it hard to draw a direct analogue to a precisely defined lattice structure, the scaling of stiffness in hollow alumina nanolattices has been shown to be fairly independent of the unit cell structure and largely influenced by the geometrical parameters of the struts.[35] Indeed, the scaling exponents calculated for the ceramic-CNT foams fall within the lower range of those reported for hollow alumina lattices (spanning $E \approx \rho^{1.41-1.83}$ and $\sigma_y \approx \rho^{1.45-1.92}$),[35] suggesting that the ceramic-CNT foams present a scaling advantage when reducing density.

Additionally, the high and sustained plateau stresses of the ceramic-CNT foams lead to large energy absorption and dissipation; combined with their low mass density, the volume-normalized energy absorption of ceramic-CNT foams exceeds hollow ceramic nanolattices[15] and other carbon-based foams[20,29,36,37] (Figure 4c). In terms of mass normalized energy absorption, CNT/graphene foams[38] have achieved higher values—237 kJ/kg at 95% strain, compared to ~50 kJ/kg at 80% strain for the best result presented in this work—but it must be noted that this value is strongly dependent on the

applied compressive strain. The ceramic-CNT foams exhibit a higher specific energy absorption at 80% compressive strain (~50 kJ/kg), compared to CNT/graphene foams (~25 kJ/kg).[38] The combination of high energy absorption capacity and recovery after large compression makes the ceramic foams especially well-suited for mechanical energy damping applications, whereas other nanoscale-architected materials either do not recover due to permanent structural damage to the struts (nanolattices) or lack comparable modulus and strength (aerogels).

In addition to the excellent strength and recovery, the alumina-coated CNT forests offer practical advantages over nanolattices. Using CNT forests as scaffolds for alumina coating allows for larger throughput production of the material (i.e., compared to 3D printed lattices), as well as the ability to tune the mechanical properties by modifying the geometric characteristics of the forest (e.g., tailoring the diameter, density, and coating properties to engineer the mechanics as predicted by the scaling models). CNT forests can be synthesized and patterned over large areas, on planar or nonplanar substrates such as advanced fibers,[39,40] and within confined geometries for packaging of delicate electrical, mechanical, or optical components. Large-scale conformal alumina coating of CNT forests can be achieved by ALD process optimization to ensure delivery of precursors to all available CNT surfaces (e.g., tuning process parameters such as deposition pressure and incorporation of flow channels through the CNT scaffold). Once the deposition process has been optimized, a roll-to-roll ALD system can be utilized for large-scale production of the final material.

CONCLUSIONS

We demonstrated that, by tailoring the balance of elastic and adhesive energies governing the deformation and contact of ceramic-coated CNTs, the resulting ultralight foams achieve strength exceeding established architected nanomaterials at similar low densities and recover more than 97% compressive strain when internal adhesive interactions are minimized. By the virtue of high and sustained plateau stress, the ceramic-CNT foams' volume-normalized energy absorption also surpasses those of other low-density materials, while preserving scaling advantage for modulus and strength. These attractive properties, in addition to the scalability of CNT growth methods to large areas, suggest that ultralight ceramic-CNT foams can be used for both structural reinforcement and mechanical damping. Moreover, CNTs are well-known for their high-temperature stability and durability, and the general principles understood here could be applied to many other engineered foam-like nanomaterials.

METHODS

CNT Growth. Micropatterned pillars of vertically aligned CNTs (CNT "forests") were fabricated from lithographically patterned catalyst on a silicon wafer. First, an array of 20 μm circles was defined on a Si wafer using standard photolithography. Then 10 nm of alumina and 1 nm of iron were deposited by electron beam evaporation (VES-2550, Temescal). The wafer was then diced to ~1 cm by 1 cm pieces. For lift-off of the photoresist, the wafer pieces were sonicated in acetone for 8 min twice with fresh acetone each time, then in isopropyl alcohol for 8 min twice also with fresh isopropyl alcohol each time, before blow drying with nitrogen. CNT growth was performed by thermal chemical vapor deposition in a quartz tube furnace with a retractable transfer arm, using the recipe described by Li et al.[41] The temperature and gas flow rates were computer-controlled, and CNT pillars were grown to ~20 μm height in 20 s at 775 °C.

Atomic Layer Deposition. Alumina was deposited onto CNTs by ALD (Gemstar, Arradiance Corporation). TMA and ozone (O_3) were used as the metalorganic and oxidizing precursors, respectively. Using nitrogen as the carrier gas at a flow rate of 40 sccm, TMA and O_3 were sequentially pulsed into the deposition chamber (2−3 Torr, 175 °C) for 22 and 100 ms, respectively. Following each precursor pulse, the chamber was purged with 90 sccm nitrogen for 38 s. This sequence was repeated for the desired number of deposition cycles on each sample.

Mechanical Testing and Imaging. The substrate with micropillars to be tested was mounted on a vertical surface facing the loading axis of a custom nanomechanical testing platform (Figure S1), which consists of a closed-loop six-degrees of freedom (6-DOF) nanopositioning stage (SmarAct) and a stiff linear piezoelectric actuator (PI), which is mounted in a scanning electron microscope (SEM). The details of the setup can be found in previous publications.[33,42] A MEMS-based load cell (FemtoTools) was installed on the 6-DOF nanopositioning stage for accurate alignment with the compression axis (the CNT forest growth direction). Displacement-controlled *in situ* compression tests were performed at constant strain rates of 10^{-3}/s, 10^{-2}/s, and 10^{-1}/s. Each CNT pillar was subjected to a full load−unload cycle, with the maximum input displacement reaching the densification regime. Load and displacement data were recorded and converted to the pillar-scale stress and strain values. SEM images were simultaneously recorded during the compressions with a 5 kV incident electron beam. The thicknesses of the ALD coatings on the CNTs were measured using TEM (Talos, Thermo Fisher Scientific) using a 200 kV primary beam.

ASSOCIATED CONTENT

ⓈI Supporting Information

The Supporting Information is available free of charge at https://pubs.acs.org/doi/10.1021/acsnano.0c02422.

> Details of the experimental setup, alumina thickness characterization, effect of e-beam exposure on recovery, pull-off force measurements, strain rate dependence of recovery, CNT unit cell description, and phase transition model (PDF)

> A video file showing excellent recovery (AVI)

AUTHOR INFORMATION

Corresponding Author

Anastasios John Hart − *Department of Mechanical Engineering, Massachusetts Institute of Technology, Cambridge, Massachusetts 02139, United States;* ⓘ orcid.org/0000-0002-7372-3512; Email: ajhart@mit.edu

Authors

Sei Jin Park − *Department of Mechanical Engineering, Massachusetts Institute of Technology, Cambridge, Massachusetts 02139, United States; Physical and Life Sciences Directorate, Lawrence Livermore National Laboratory, Livermore, California 94550, United States;* ⓘ orcid.org/0000-0001-6877-1512

Jungho Shin − *Materials Department, University of California Santa Barbara, Santa Barbara, California 93106, United States*

Daniel J. Magagnosc − *Materials Science and Engineering, University of Pennsylvania, Philadelphia, Pennsylvania 19104, United States*

Sanha Kim − *Department of Mechanical Engineering, Massachusetts Institute of Technology, Cambridge,*

Massachusetts 02139, United States; ● orcid.org/0000-0002-3548-6173

Changhong Cao − *Department of Mechanical Engineering, Massachusetts Institute of Technology, Cambridge, Massachusetts 02139, United States*

Kevin T. Turner − *Department of Mechanical Engineering and Applied Mechanics, University of Pennsylvania, Philadelphia, Pennsylvania 19104, United States;* ● orcid.org/0000-0003-4963-4568

Prashant K. Purohit − *Department of Mechanical Engineering and Applied Mechanics, University of Pennsylvania, Philadelphia, Pennsylvania 19104, United States*

Daniel S. Gianola − *Materials Department, University of California Santa Barbara, Santa Barbara, California 93106, United States*

Complete contact information is available at:
https://pubs.acs.org/10.1021/acsnano.0c02422

Notes

The authors declare no competing financial interest.

REFERENCES

(1) Loh, Q.; Choong, C. Three-Dimensional Scaffolds for Tissue Engineering Applications: Role of Porosity and Pore Size. *Tissue Eng., Part B* **2013**, *19*, 485−502.

(2) Feng, J.; Feng, J.; Jiang, Y.; Zhang, C. Ultralow Density Carbon Aerogels with Low Thermal Conductivity up to 2000 Degrees C. *Mater. Lett.* **2011**, *65*, 3454−3456.

(3) Zhao, Y.; Hu, C.; Hu, Y.; Cheng, H.; Shi, G.; Qu, L. A Versatile, Ultralight, Nitrogen-Doped Graphene Framework. *Angew. Chem., Int. Ed.* **2012**, *51*, 11371−11375.

(4) Hashim, D.; Narayanan, N.; Romo-Herrera, J.; Cullen, D.; Hahm, M.; Lezzi, P.; Suttle, J.; Kelkhoff, D.; Munoz-Sandoval, E.; Ganguli, S.; Roy, A.; Smith, D.; Vajtai, R.; Sumpter, B.; Meunier, V.; Terrones, H.; Terrones, M.; Ajayan, P., Covalently Bonded Three-Dimensional Carbon Nanotube Solids *via* Boron Induced Nanojunctions. *Sci. Rep.* **2012**, *2*. DOI: 10.1038/srep00363

(5) Wujcik, E.; Monty, C. Nanotechnology for Implantable Sensors: Carbon Nanotubes and Graphene in Medicine. *Wiley Interdiscip. Rev.: Nanomed. Nanobiotechnol.* **2013**, *5*, 233−249.

(6) Chen, Z.; Ren, W.; Gao, L.; Liu, B.; Pei, S.; Cheng, H. Three-Dimensional Flexible and Conductive Interconnected Graphene Networks Grown by Chemical Vapour Deposition. *Nat. Mater.* **2011**, *10*, 424−428.

(7) Zhuo, H.; Hu, Y. J.; Tong, X.; Chen, Z. H.; Zhong, L. X.; Lai, H. H.; Liu, L. X.; Jing, S. S.; Liu, Q. Z.; Liu, C. F.; Peng, X. W.; Sun, R. C. A Supercompressible, Elastic, and Bendable Carbon Aerogel with Ultrasensitive Detection Limits for Compression Strain, Pressure, and Bending Angle. *Adv. Mater.* **2018**, *30*, 9.

(8) Bi, H.; Lin, T. Q.; Xu, F.; Tang, Y. F.; Liu, Z. Q.; Huang, F. Q. New Graphene Form of Nanoporous Monolith for Excellent Energy Storage. *Nano Lett.* **2016**, *16*, 349−354.

(9) Zheng, X. Y.; Lee, H.; Weisgraber, T. H.; Shusteff, M.; DeOtte, J.; Duoss, E. B.; Kuntz, J. D.; Biener, M. M.; Ge, Q.; Jackson, J. A.; Kucheyev, S. O.; Fang, N. X.; Spadaccini, C. M. Ultralight, Ultrastiff Mechanical Metamaterials. *Science* **2014**, *344*, 1373−1377.

(10) Zheng, X. Y.; Smith, W.; Jackson, J.; Moran, B.; Cui, H. C.; Chen, D.; Ye, J. C.; Fang, N.; Rodriguez, N.; Weisgraber, T.; Spadaccini, C. M. Multiscale Metallic Metamaterials. *Nat. Mater.* **2016**, *15*, 1100−1106.

(11) Gao, H. J.; Ji, B. H.; Jager, I. L.; Arzt, E.; Fratzl, P. Materials Become Insensitive to Flaws at Nanoscale: Lessons from Nature. *Proc. Natl. Acad. Sci. U. S. A.* **2003**, *100*, 5597−5600.

(12) Cao, A. Y.; Dickrell, P. L.; Sawyer, W. G.; Ghasemi-Nejhad, M. N.; Ajayan, P. M. Super-Compressible Foamlike Carbon Nanotube Films. *Science* **2005**, *310*, 1307−1310.

(13) Kucheyev, S.; Stadermann, M.; Shin, S.; Satcher, J.; Gammon, S.; Letts, S.; van Buuren, T.; Hamza, A. Super-Compressibility of Ultralow-Density Nanoporous Silica. *Adv. Mater.* **2012**, *24*, 776−780.

(14) Schaedler, T. A.; Jacobsen, A. J.; Torrents, A.; Sorensen, A. E.; Lian, J.; Greer, J. R.; Valdevit, L.; Carter, W. B. Ultralight Metallic Microlattices. *Science* **2011**, *334*, 962−965.

(15) Meza, L. R.; Das, S.; Greer, J. R. Strong, Lightweight, and Recoverable Three-Dimensional Ceramic Nanolattices. *Science* **2014**, *345*, 1322−1326.

(16) Meaud, J.; Sain, T.; Yeom, B.; Park, S. J.; Shoultz, A. B.; Hulbert, G.; Ma, Z. D.; Kotov, N. A.; Hart, A. J.; Arruda, E. M.; Waas, A. M. Simultaneously High Stiffness and Damping in Nanoengineered Microtruss Composites. *ACS Nano* **2014**, *8*, 3468−3475.

(17) Bauer, J.; Hengsbach, S.; Tesari, I.; Schwaiger, R.; Kraft, O. High-Strength Cellular Ceramic Composites with 3D Microarchitecture. *Proc. Natl. Acad. Sci. U. S. A.* **2014**, *111*, 2453−2458.

(18) Brieland-Shoultz, A.; Tawfick, S.; Park, S. J.; Bedewy, M.; Maschmann, M. R.; Baur, J. W.; Hart, A. J. Scaling the Stiffness, Strength, and Toughness of Ceramic-Coated Nanotube Foams into the Structural Regime. *Adv. Funct. Mater.* **2014**, *24*, 5728−5735.

(19) Stano, K.; Faraji, S.; Yildiz, O.; Akyildiz, H.; Bradford, P.; Jur, J. Strong and Resilient Alumina Nanotube and CNT/Alumina Hybrid Foams with Tuneable Elastic Properties. *RSC Adv.* **2017**, *7*, 27923−27931.

(20) Bradford, P. D.; Wang, X.; Zhao, H. B.; Zhu, Y. T. Tuning the Compressive Mechanical Properties of Carbon Nanotube Foam. *Carbon* **2011**, *49*, 2834−2841.

(21) Fan, S. S.; Chapline, M. G.; Franklin, N. R.; Tombler, T. W.; Cassell, A. M.; Dai, H. J. Self-Oriented Regular Arrays of Carbon Nanotubes and Their Field Emission Properties. *Science* **1999**, *283*, 512−514.

(22) Bedewy, M.; Meshot, E. R.; Guo, H. C.; Verploegen, E. A.; Lu, W.; Hart, A. J. Collective Mechanism for the Evolution and Self-Termination of Vertically Aligned Carbon Nanotube Growth. *J. Phys. Chem. C* **2009**, *113*, 20576−20582.

(23) Pathak, S.; Mohan, N.; Decolvenaere, E.; Needleman, A.; Bedewy, M.; Hart, A. J.; Greer, J. R. Local Relative Density Modulates Failure and Strength in Vertically Aligned Carbon Nanotubes. *ACS Nano* **2013**, *7*, 8593−8604.

(24) Park, S. J.; Schmidt, A. J.; Bedewy, M.; John Hart, A. Measurement of Carbon Nanotube Microstructure Relative Density by Optical Attenuation and Observation of Size-Dependent Variations. *Phys. Chem. Chem. Phys.* **2013**, *15*, 11511−11519.

633 (25) Gibson, L.; Ashby, M. *Cellular Solids: Structure and Properties,* 2
634 nd ed.; Cambridge Solid State Science Series; Cambridge University
635 Press: Cambridge, England, 1999.

636 (26) Falvo, M. R.; Clary, G. J.; Taylor, R. M.; Chi, V.; Brooks, F. P.;
637 Washburn, S.; Superfine, R. Bending and Buckling of Carbon
638 Nanotubes under Large Strain. *Nature* **1997**, *389*, 582−584.

639 (27) Yakobson, B. I.; Brabec, C. J.; Bernholc, J. Nanomechanics of
640 Carbon Tubes: Instabilities beyond Linear Response. *Phys. Rev. Lett.*
641 **1996**, *76*, 2511−2514.

642 (28) Yakobson, B. I.; Campbell, M. P.; Brabec, C. J.; Bernholc, J.
643 High Strain Rate Fracture and C-Chain Unraveling in Carbon
644 Nanotubes. *Comput. Mater. Sci.* **1997**, *8*, 341−348.

645 (29) Pathak, S.; Lim, E. J.; Pour Shahid Saeed Abadi, P.; Graham, S.;
646 Cola, B. A.; Greer, J. R. Higher Recovery and Better Energy
647 Dissipation at Faster Strain Rates in Carbon Nanotube Bundles: An
648 *In-Situ* Study. *ACS Nano* **2012**, *6*, 2189−2197.

649 (30) Won, Y.; Gao, Y.; Panzer, M. A.; Xiang, R.; Maruyama, S.;
650 Kenny, T. W.; Cai, W.; Goodson, K. E. Zipping, Entanglement, and
651 the Elastic Modulus of Aligned Single-Walled Carbon Nanotube
652 Films. *Proc. Natl. Acad. Sci. U. S. A.* **2013**, *110*, 20426−20430.

653 (31) Israelachvili, J. N. *Intermolecular and Surface Forces,* 3 rd ed.;
654 Academic Press: San Diego, CA, 2011.

655 (32) Yaglioglu, O.; Cao, A. Y.; Hart, A. J.; Martens, R.; Slocum, A.
656 H. Wide Range Control of Microstructure and Mechanical Properties
657 of Carbon Nanotube Forests: A Comparison Between Fixed and
658 Floating Catalyst CVD Techniques. *Adv. Funct. Mater.* **2012**, *22*,
659 5028−5037.

660 (33) Liang, X.; Shin, J.; Magagnosc, D.; Jiang, Y.; Jin Park, S.; John
661 Hart, A.; Turner, K.; Gianola, D. S.; Purohit, P. K. Compression and
662 Recovery of Carbon Nanotube Forests Described as a Phase
663 Transition. *Int. J. Solids Struct.* **2017**, *122*, 196−209.

664 (34) Rayneau-Kirkhope, D.; Mao, Y.; Farr, R. Ultralight Fractal
665 Structures from Hollow Tubes. *Phys. Rev. Lett.* **2012**, *109*, 204301.

666 (35) Meza, L. R.; Phlipot, G. P.; Portela, C. M.; Maggi, A.;
667 Montemayor, L. C.; Comella, A.; Kochmann, D. M.; Greer, J. R.
668 Reexamining the Mechanical Property Space of Three-Dimensional
669 Lattice Architectures. *Acta Mater.* **2017**, *140*, 424−432.

670 (36) Misra, A.; Raney, J. R.; De Nardo, L.; Craig, A. E.; Daraio, C.
671 Synthesis and Characterization of Carbon Nanotube-Polymer Multi-
672 layer Structures. *ACS Nano* **2011**, *5*, 7713−7721.

673 (37) Kim, K. H.; Oh, Y.; Islam, M. F. Graphene Coating Makes
674 Carbon Nanotube Aerogels Superelastic and Resistant to Fatigue.
675 *Nat. Nanotechnol.* **2012**, *7*, 562−566.

676 (38) Tang, C.; Zhang, Q.; Zhao, M. Q.; Tian, G. L.; Wei, F. Resilient
677 Aligned Carbon Nanotube/Graphene Sandwiches for Robust
678 Mechanical Energy Storage. *Nano Energy* **2014**, *7*, 161−169.

679 (39) Yamamoto, N.; John Hart, A.; Garcia, E. J.; Wicks, S. S.;
680 Duong, H. M.; Slocum, A. H.; Wardle, B. L. High-Yield Growth and
681 Morphology Control of Aligned Carbon Nanotubes on Ceramic
682 Fibers for Multifunctional Enhancement of Structural Composites.
683 *Carbon* **2009**, *47*, 551−560.

684 (40) Polsen, E. S.; Stevens, A. G.; Hart, A. J. Laser Printing of
685 Nanoparticle Toner Enables Digital Control of Micropatterned
686 Carbon Nanotube Growth. *ACS Appl. Mater. Interfaces* **2013**, *5*,
687 3656−3662.

688 (41) Li, J. J.; Bedewy, M.; White, A. O.; Polsen, E. S.; Tawfick, S.;
689 Hart, A. J. Highly Consistent Atmospheric Pressure Synthesis of
690 Carbon Nanotube Forests by Mitigation of Moisture Transients. *J.*
691 *Phys. Chem. C* **2016**, *120*, 11277−11287.

692 (42) Magagnosc, D. J.; Kumar, G.; Schroers, J.; Felfer, P.; Cairney, J.
693 M.; Gianola, D. S. Effect of Ion Irradiation on Tensile Ductility,
694 Strength and Fictive Temperature in Metallic Glass Nanowires. *Acta*
695 *Mater.* **2014**, *74*, 165−182.